High Power Laser Science and Engineering, (2024), Vol. 12, e47, 11 pages.
doi:10.1017/hpl.2024.28

HIGH POWER LASER SCIENCE AND ENGINEERING

RESEARCH ARTICLE

The influence of space environmental factors on the laser-induced damage thresholds in optical components

Bin Ma[1,2,3,4], Shuang Guan[1,2], Dongyue Yan[1,2], Qiaofei Pan[1,2], Zhiqiang Hou[1,2], Ke Wang[1,2], and Jiaqi Han[1,2]

[1] *Institute of Precision Optical Engineering, School of Physics Science and Engineering, Tongji University, Shanghai, China*

[2] *MOE Key Laboratory of Advanced Micro-Structured Materials, Tongji University, Shanghai, China*

[3] *Shanghai Frontiers Science Center of Digital Optics, Tongji University, Shanghai, China*

[4] *Shanghai Professional Technical Service Platform for Full-Spectrum and High-Performance Optical Thin Film Devices and Applications, Tongji University, Shanghai, China*

(Received 11 December 2023; revised 11 March 2024; accepted 29 April 2024)

Abstract

This paper systematically investigated the impact mechanisms of proton irradiation, atomic oxygen irradiation and space debris collision, both individually and in combination, on the laser damage threshold and damage evolution characteristics of HfO_2/SiO_2 triple-band high-reflection films and fused silica substrates using a simulated near-Earth space radiation experimental system. For the high-reflection film samples, the damage thresholds decreased by 15.38%, 13.12% and 46.80% after proton, atomic oxygen and simulated space debris (penetration) irradiation, respectively. The coupling irradiation of the first two factors resulted in a decrease of 26.93%, while the combined effect of all the three factors led to a reduction of 63.19%. Similarly, the fused silica substrates exhibited the same pattern of laser damage performance degradation. Notably, the study employed high-precision fixed-point *in situ* measurement techniques to track in detail the microstructural changes, surface roughness and optical-thermal absorption intensity before and after proton and atomic oxygen irradiation at the same location, thus providing a more accurate and comprehensive analysis of the damage mechanisms. In addition, simulations were conducted to quantitatively analyze the transmission trajectories and concentration distribution lines of protons and atomic oxygen incident at specific angles into the target material. The research findings contribute to elucidating the laser damage performance degradation mechanism of transmissive elements in near-Earth space environments and provide technical support for the development of high-damage-threshold optical components resistant to space radiation.

Keywords: coupling effects; laser-induced damage thresholds; optical components; space environments

1. Introduction

In near-Earth and space environments, the performance stability and service life of optical components used in laser systems are significantly diminished by the conditions of outer space[1,2]. Multiple research institutions have conducted space flight tests and ground-based accelerated simulation experiments to investigate changes in thin film performance during exposure to space. For instance, degradation in spectral performance and changes in surface morphology were observed in thin films during multiple flight tests and experiments on the International Space Station[3,4]. Researchers have also conducted specialized space environment tests on various optical materials using ground-based facilities, yielding a wealth of experimental data[5,6]. Previous studies on near-Earth space environments have produced several related results, as explained below. (1) Differences in membrane layer thermal conductivity and heat transfer in high vacuum conditions (~10^{-7} Pa)[7] reduce thin film damage thresholds when laser-induced damage occurs, as compared with atmospheric environments. (2) High–low temperature cycling (from approximately −80°C to 120°C)[8] causes issues such as film delamination, due to differences in thermal expansion coefficients between the film and the crystal. Even constant low temperatures can decrease temperature rising in the laser irradiation region, thereby increasing component damage thresholds[9]. (3) Solar ultraviolet radiation[10,11], especially high-energy ultraviolet photons with wavelengths of less than 200 nm (capable of breaking chemical bonds in polymer materials), can

Correspondence to: B. Ma, Institute of Precision Optical Engineering, School of Physics Science and Engineering, Tongji University, Shanghai 200092, China. Email: mabin@tongji.edu.cn

significantly reduce thin film transmittance. (4) Atomic oxygen[12] can exhibit orbital speeds of 8 km/s, with head-on flux densities reaching 10^{15} atoms/(cm^2·s) and kinetic energies of approximately 5 eV. Associated effects include reactive sputtering and surface erosion, leading to an increase in film surface roughness, microstructure damage and even delamination[13]. (5) Charged particles[14] must also be considered, consisting primarily of protons (<50 MeV) and electrons (~0.5 MeV) from Earth's radiation belts, in addition to galactic cosmic rays (primarily protons and various heavy ions with flux densities of a few/(cm^2·s) and energies in the range of 0.5–100 GeV) and solar cosmic rays (primarily protons with energies below 1 GeV, accompanied by alpha particles and heavy nuclei). The flux of these charged particles is closely related to factors such as orbital altitude and particle energy. Proton energy typically increases as flux decreases. This primarily leads to ionizing effects and radiation damage, due to atomic (or ionic) displacement, as well as single particle effects resulting from high-energy particle impacts on microelectronic devices or changes in state. (6) Micrometeoroids and space debris[15] are additional factors present in space environments. Micrometeoroids are high-speed moving matter in cosmic space (with average speeds of ~20 km/s), while space debris consists of discarded spacecraft and their fragments (with average speeds of ~10 km/s). The quantity of both decreases rapidly as mass and diameter increase. Particles smaller than 0.1 mm corrode spacecraft surfaces, while particles larger than 1 mm cause severe damage. In addition, various types of radiation exposure may cause ionizing damage and organic material volatilization, leading to contamination[16].

The transmissive window components at the forefront of laser radar systems are primarily prepared by physical methods such as electron beam (EB) evaporation and ion beam sputtering (IBS)[17,18]. High vacuum and solar ultraviolet radiation have a relatively minor influence on these components due to dense film structures, stable mechanical strength, good mechanical properties and thermal parameters[19,20]. The creation of defects, such as color centers generated by low energy charged particles, can form absorption bands of different wavelengths, leading to material optical performance degradation and reduced transmittance[16]. Burnham *et al.*[21] and Demos *et al.*[22] have shown that the vacuum environment reduces the transmittance of fused silica and the surface of the film reflection layer and increases the probability of catastrophic damage. The impact of vacuum on optical components primarily manifests in alterations of thermal parameters, leading to easier heat accumulation and subsequent damage. This exacerbates the irradiation of initial damage areas, resulting in larger and more severe damage. The effects of atomic oxygen on thin film oxidation-reduction processes are approximately negligible during controlled oxygenation, since thin film materials are generally oxides (e.g., HfO_2/SiO_2)[23]. In addition, the primary structures of current laser radar systems often undergo optimization, sealing, shielding and constant temperature control, thus minimizing the effects of thermal cycling and extensive volatile contamination. Atomic oxygen and high-energy protons, colliding directly with laser radar systems, can disrupt thin film surfaces and internal lattice structures through bombardment sputtering and penetration, potentially causing micro-nano-structural damage to the thin film and substrate. Micro-damage resulting from space debris impacts is highly likely to become a trigger site for laser-induced damage, especially when transmissive components are subjected to prolonged laser exposure.

In summary, micro-nano-scale damage structures resulting from atomic oxygen and high-energy proton bombardment (in addition to impacts from micrometeoroids and space debris)[24,25] can intensify the modulation of laser optical field distributions[26]. Furthermore, their lower structural strength, internal material fractures and resulting increases in absorption coefficients (due to changes in the energy bandgap width[27]) suggest that even minute damage may appear under the influence of multi-pulse lasers, leading to persistent damage growth. Consequently, this paper explores degradation patterns and mechanisms of laser-induced damage to optical components in near-Earth and space environments. Detrimental surface effects caused by various environmental factors, problematic irradiation conditions, the coupled relationship between them and corresponding laser-induced damage thresholds (LIDTs) are also discussed.

2. Experimental setup

2.1. LIDT testing

An LIDT testing system was established using a Spectra Physics neodymium-doped yttrium aluminum garnet (Nd:YAG) laser[28]. The output mode was characterized as TEM_{00}, operating at a wavelength of 1064 nm, with a pulse width of 10 ns and a repetition rate of 10 Hz. In the LIDT test, the combination of a λ/2 wave plate and a polarizing beam splitter (PBS) allows for an energy adjustment range of 340 μJ–70 mJ @ 1064 nm (equivalent to an energy density adjustment range of 1–200 J/cm² @ 1064 nm). The beam diameter at 1/e² intensity after focusing by a lens with a focal length of 1 m is 210 μm. This system included energy regulation, focusing and damage monitoring regions. Real-time observations were made using a HIROX long-distance microscope equipped with 70×–700× objective lenses. A charge-coupled device (CCD; SP620U, Spiricon) was also employed to achieve micrometer-scale imaging resolution, thereby enabling online observations. Offline inspection was performed using differential interference microscopy, utilized to accurately ascertain laser damage and collect corresponding data. Several methods were employed

during the experiments to determine the LIDT of optical components, including S-on-1, R-on-1 and raster scanning. Specifically, S-on-1 ($S = 10$) testing results were indicated by a zero-probability damage threshold. In the R-on-1 process, minimal 20 test points were selected for each sample. The calculated average of all data was considered the damage threshold, along with the corresponding standard deviation. The raster scanning included comprehensive imaging of test samples, thereby providing a technique that best captured the impact of defects on optical component LIDTs, despite requiring the longest runtime.

2.2. Sample preparation

The choice of substrates is crucial in space environments. Compared to diamond and silicon (Si), fused silica material is widely chosen as the substrate material for optical components in space environments due to its high transmittance, high damage threshold, excellent radiation resistance and ease of optical processing in the 300–1100 nm wavelength range, particularly in the Nd:YAG laser wavelength band[29–34]. As such, high-reflection thin films fabricated on fused silica substrates were selected as experimental samples in this study because coatings produced by this method exhibit higher damage thresholds under nanosecond pulses[35–37].

(1) High-reflection thin films

High-reflection tri-band thin films (1064/532/355 nm) were deposited on $\varphi 30 \times 5$ mm substrates using an EB evaporation process. The reflective coatings employed a HfO_2/SiO_2 film stack totaling 79 layers and structured as 0.327 (0.8H 1.2L) ^{17} (0.7H 1.3L) ^{22} L. Here, 'H' represents a HfO_2 monolayer with a quarter-wavelength thickness and a 45° angle of incidence, while 'L' denotes a SiO_2 monolayer with a quarter-wavelength thickness and the same angle of incidence. The term '0.327' signifies a central wavelength at 0.327L using an angle of 45°.

(2) Fused silica substrate

The fused silica samples ($\varphi 30$ mm) were ground and polished using SiC abrasives and CeO_2 powder of varying sizes and removal depths. Atomic force microscopy (AFM) measurements indicated a surface roughness of approximately 0.45 nm.

2.3. Space irradiation experiment simulation

Space radiation environments are characterized by orbital properties, with key parameters for low Earth orbit (LEO) satellites including altitude and inclination. Consequently, once these conditions are established, the space environment in which the satellite will operate is fundamentally determined. The space radiation experiments in this paper involved ground simulations conducted at the Beijing Institute of Spacecraft Environment Engineering. Proton and atomic oxygen radiation parameters were established in conjunction with a radiation apparatus, designed based on the actual radiation flux experienced by spacecraft during a year at near-Earth orbit altitudes. In addition, an R-on-1 damage testing method was employed to consider factors affecting a space environment. This approach simulated three different typical effects resulting from the high-speed impacts of tiny fragments or micro-nano-scale contaminants on the sample surface. This involved penetration holes, compression-induced cracking and cratering, included to further analyze the influence of various impact effects on the LIDT and damage evolution materials.

(1) Proton irradiation effect simulations

The effects of proton irradiation on high-reflection thin films and fused silica substrates were investigated using a ground-based space environment simulation facility. These experiments involved a comprehensive irradiation test device ($\varphi 800$ mm) and corresponding apparatus with a vacuum level ranging between 3.5×10^{-4} and 5×10^{-4} Pa, with a 10% beam nonuniformity and 4% beam instability. The sample platform was temperature controlled at 25°C. Proton irradiation energy was set to 40 keV, with a low-energy proton flux of 2.5×10^9 protons/(cm^2·s) and an accumulated flux of 1.0×10^{13} protons/cm^2. The entire 30 mm diameter sample underwent comprehensive irradiation.

(2) Atomic oxygen irradiation effect simulations

In near-Earth orbits, the static density of atomic oxygen ranges from 5×10^6 to 5×10^9 atoms/cm^3 at different altitudes. However, for spacecraft traveling at velocities of approximately 8 km/s, atomic oxygen collides with the spacecraft surface at a relative flux ranging from 10^{12} to 10^{15} atoms/(cm^2·s), with a kinetic energy of 5 eV. This process induces multiple chemical and physical reactions. Parameters for the ground-based atomic oxygen simulation equipment were established in conjunction with the irradiation apparatus and selected based on the actual radiation flux experienced by spacecraft during an annual orbit. The atomic oxygen flux was assumed to be 5×10^{15} atoms/(cm^2·s), with an accumulated flux of 5.0×10^{20} atoms/cm^2 and an energy level of 5 eV.

(3) Simulating the effects of microscopic fragment impacts

Penetration holes – A coherent Astrella Ti sapphire pulsed laser system was utilized to create laser-produced micro-holes. This system generated a TEM_{00} mode laser with a maximum output power of 7 W, operating at a frequency of 1 kHz, with a central wavelength of 800 nm and a pulse width of 35 fs. Holes with diameters of approximately 30 μm were generated by adjusting the laser power, as shown in Figure 1(a), producing 20–30 data points.

Compression-induced cracking – Samples exhibiting compression-induced cracks were prepared using a microhardness indenter. A circular press head was used to

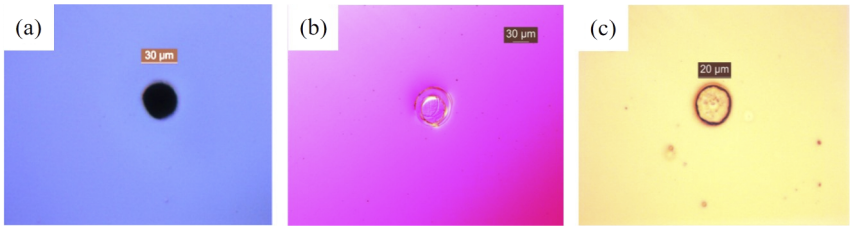

Figure 1. Simulated impacts from different types of microscopic fragments: (a) penetration holes, (b) compression-induced cracking and (c) cratering.

apply pressure for 3 seconds with a force of 980 mN, creating impressions with diameters of approximately 30 μm, as illustrated in Figure 1(b).

Cratering – A Nd:YAG nanosecond laser with a maximum energy output of 2 J, operating in TEM_{00} mode at a frequency of 10 Hz, was used to replicate cratering effects. The experimental wavelength was 355 nm, while the pulse width was 8 ns. Craters with diameters of approximately 30 μm were produced by modulating the laser power, as presented in Figure 1(c).

3. The impact of environmental factors on laser damage performance

The emergence of triggers susceptible to laser damage (on the surface of optical components) can initiate failure structures, which may grow and eventually cause the failure of an entire system when exposed to subsequent high-energy pulse lasers. Since near-Earth space environments are extremely complex and harsh, understanding and mastering the effects of different environmental factors on transmission components is critical for damage factor identification. In this section, the LIDT and damage evolution of three-wavelength high-reflectance films and fused silica substrates will be analyzed under the separate influence of three environmental factors: atomic oxygen irradiation, proton irradiation and space debris impacts. Differences between various debris types and sizes will also be discussed.

3.1. Effects of atomic oxygen irradiation

(1) LIDT results for high-reflection films

The LIDT for high-reflection films was measured using three different methods at a working wavelength of 1064 nm, before and after exposure to atomic oxygen. LIDT values before and after irradiation were determined using the S-on-1 ($S = 10$) method to be 65.73 and 44.06 J/cm^2, respectively, representing a reduction of 32.96%. Similarly, employing the R-on-1 technique produced LIDT values of 141.30 and 122.75 J/cm^2 (before and after irradiation), representing a reduction of 13.12%. LIDT measurements collected with a raster scan were 46.74 and 24.66 J/cm^2, indicating a reduction of 47.24%. These results suggested that the LIDT for highly reflective films decreased notably after exposure to atomic oxygen.

(2) LIDT results for fused silica substrates

Similarly, LIDTs measured before and after irradiation, using the S-on-1 method, were 64.01 and 63.11 J/cm^2, respectively, demonstrating a decrease of 1.4%. Likewise, the R-on-1 method produced LIDTs of 130.43 and 112.24 J/cm^2, a reduction of 13.94%. LIDTs measured with a raster scan were 44.56 and 14.75 J/cm^2, a reduction of 66.89%. This suggests the LIDT of fused silica substrates decreased significantly after exposure to atomic oxygen.

Two reasons contribute to the higher damage threshold of high-reflection coatings compared with substrates[38]: (1) the formation of subsurface structures on the surface of optical elements due to mechanical processes such as grinding and polishing during fabrication, leading to a decrease in the damage threshold; (2) the formation of a standing wave electric field in high-reflection coatings under laser irradiation, with damage initiating from the interfaces of the film layers.

3.2. Study on the effects of proton irradiation

(1) LIDT results for high-reflection films

A series of LIDT values was obtained before and after proton irradiation at a working wavelength of 1064 nm using three measurement techniques, representing a significant reduction in three-band reflectance after exposure to 40 keV protons. Specifically, LIDTs measured using the S-on-1 method (before and after irradiation) were 67.06 and 52.36 J/cm^2, respectively. The R-on-1 technique produced LIDTs of 141.30 and 119.56 J/cm^2, while a raster scan yielded 46.74 and 41.30 J/cm^2.

(2) LIDT results for fused silica substrates

LIDTs were measured before and after proton irradiation using the S-on-1 method, producing values of 64.01 and 48.59 J/cm^2, respectively, representing a reduction of 24.08%. The R-on-1 method produced LIDT values of 130.43 and 105.01 J/cm^2, a decrease of 19.48%. Employing a raster scan yielded 44.56 and 34.78 J/cm^2, a reduction of 21.94%.

3.3. Effects of microscopic fragment impacts

The R-on-1 testing method was also used to assess the effect of fragment impacts on LIDT and damage evolution in optical thin films. A test wavelength of 1064 nm was

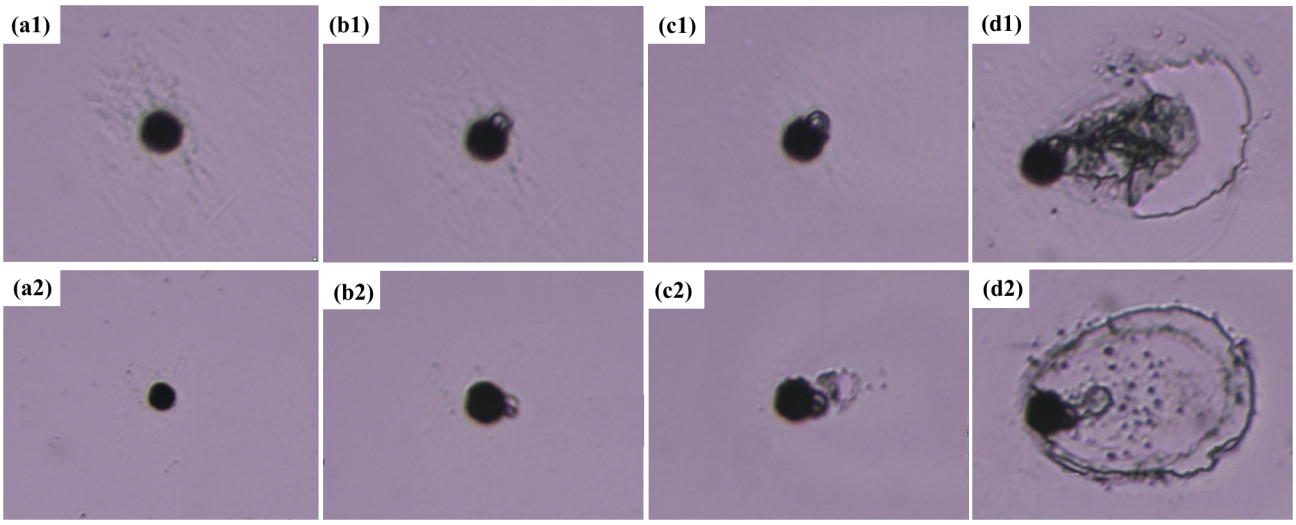

Figure 2. Damage condition of high-reflectance thin film (one series) and substrate (two series) samples: (a) initial damage morphology; (b) damage to the membrane around the hole; (c) bright spots appearing around the hole; (d) extensive damage centered around the hole.

employed, with an energy gradient controlled by rotating a waveplate to adjust the nanosecond laser energy. Tests were performed on holes of various sizes in the high-reflectance film and substrate samples, as shown in Figure 2. At least 20 test points were selected from each sample and the evolution of the damage state was recorded during energy increase and corresponding energy density fluctuation. The average value of the energy density in a given state served as the LIDT measurement. Four primary damage states were predominantly observed during energy increase in the high-reflectance film samples. No significant laser damage was initially observed at very low energy densities. However, the upper-right region of the film exhibited some peeling near the laser incidence direction. Evidence of damage inside the holes then increased with the energy level, as areas of peeling expanded further. A prominent bright spot then appeared on the right-hand side of the hole, demonstrating apparent directionality related to the 45° angle between the laser incidence direction and the sample surface. As the laser energy increased further, catastrophic damage became evident around the hole, exhibiting a typical 45° incident damage morphology.

Applying the R-on-1 testing method to substrate samples produced a similar damage evolution with increasing energy, similar to that of high-reflectance film samples. This final state showed signs of large-area peeling, consistent with high-reflectance films. However, the threshold corresponding to each damage state differed from that of high-reflectance films, as depicted by the test results shown in Figure 3. Likewise, the simulated effects of compression-induced cracking and cratering, representing the impacts of fragment strikes, exerted a similar influence on the high-reflection film and fused silica substrates.

In summary, an experimental analysis was conducted to determine the LIDTs of three-waveband high-reflectance

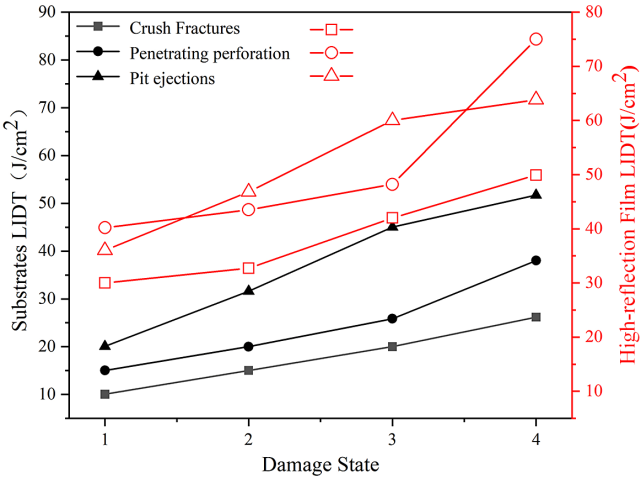

Figure 3. LIDT results for different states in 30 μm substrates and high-reflection films (1, initial damage morphology; 2, damage to the membrane around the hole; 3, bright spots appearing around the hole; 4, extensive damage centered around the hole).

films and fused silica substrates under the independent actions of three space environment factors: atomic oxygen exposure, proton irradiation and space debris impacts. These results, acquired from 30 μm impact samples, were compared using R-on-1 testing, as depicted in Figures 4 and 5. It is evident from the figures that LIDT values for both high-reflectance films and substrates significantly decreased under the influence of these environmental factors. Notably, impacts from space debris exhibited the most pronounced effects. Among the three distinct impact morphologies, samples with crush fractures displayed the lowest values. This can be attributed to material fracturing induced by debris collisions, which enhanced the modulation of electric fields around the edges and created new absorption sources at the discontinuous interface. Consequently, a reduction in

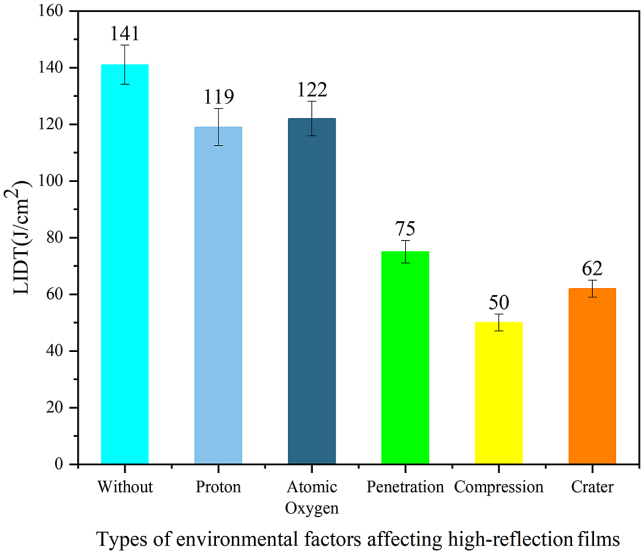

Figure 4. A comparison of LIDTs for high-reflection films under the action of single space environmental factors ('Without' represents being without any space environmental factors).

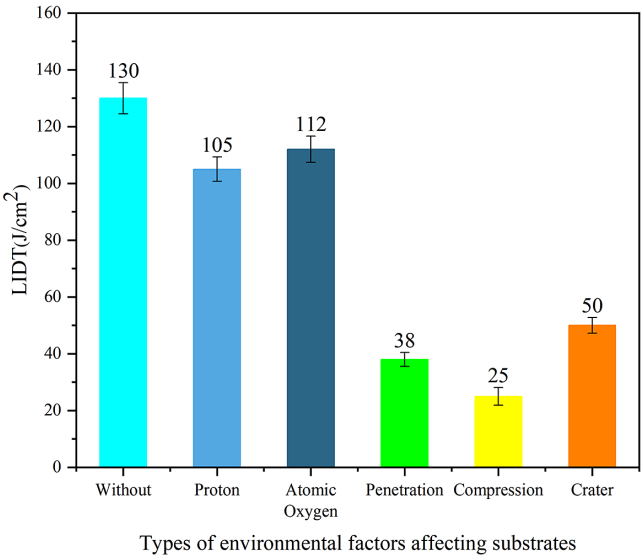

Figure 5. A comparison of LIDTs for substrates under the action of single space environmental factors ('Without' represents being without any space environmental factors).

resistance to laser damage and proton erosion occurred due to the severity of material fractures, which were closely related to associated damage resistance capabilities[9]. These crushed samples displayed the largest and most distinct material fractures, making them more prone to damage from laser irradiation and thus producing the lowest LIDTs.

4. Coupled effects of space environmental factors on laser damage performance

Due to the complex nature of space missions, materials are concurrently subjected to various environmental factors, including atomic oxygen, protons, space debris,

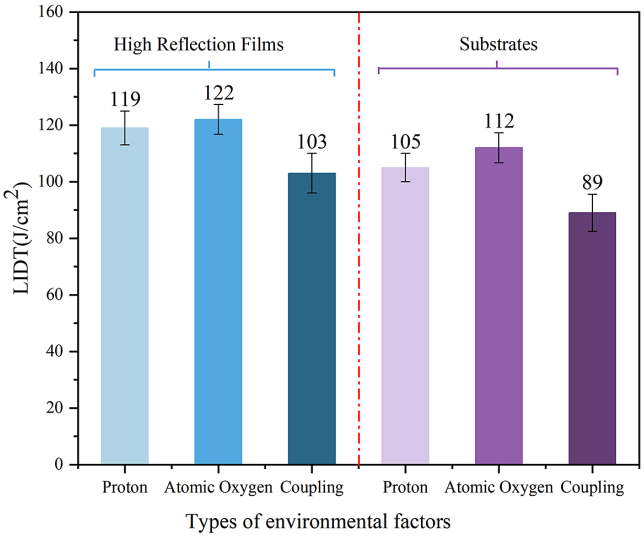

Figure 6. A comparison of LIDT values produced by the coupled effect of atomic oxygen and protons.

contamination and temperature extremes. The interactions among these elements contribute to mutual influence effects. As such, only through the study of the coupling of multiple factors can an accurate and reliable assessment of optical components be achieved. While extensive research has been conducted internationally on the effects of individual mechanisms, studies on the combined effects of multiple conditions are somewhat limited. As such, this section builds on experiments that have individually examined the influence of protons, atomic oxygen and space debris on laser damage performance in high-reflectance films and substrates. The focus of this work is to investigate various combinations of factors to better understand coupling effects and associated laser damage performance. This is done by investigating different combined states, including protons and space debris, atomic oxygen and space debris, protons and atomic oxygen and the combination of protons, atomic oxygen and space debris.

4.1. Coupled effects of protons and atomic oxygen

Figure 6 provides a comparison of LIDT values for coupling versus individual effects from protons and atomic oxygen. The horizontal axis represents three different modes of action: proton irradiation alone, atomic oxygen irradiation alone and the coupled impact of atomic oxygen and protons. The vertical axis represents LIDTs for each sample. Table 1 presents a comparison of reductions in the LIDT for different modes of action. An analysis of these images suggests the effects of atomic oxygen and protons on sample LIDT values were similar, with proton irradiation slightly more pronounced than atomic oxygen irradiation. Among these results, the coupled effect of atomic oxygen and protons had the greatest impact on sample LIDTs, indicating this combination mutually enhanced destructive capabilities.

Table 1. A comparison of LIDT reductions for different modes of action.

Sample type	LIDT reduction		
	Protons	Atomic oxygen	Protons & atomic oxygen
High–reflectance films	15.38%	13.12%	26.93%
Substrates	19.48%	18.19%	41.09%

The experimental results in Figures 4 and 5 are consistent with the coupling effects of space debris with either protons or atomic oxygen, which were more significant than the combined effect of both. This outcome was consistent with the preceding results.

4.2. Influence of coupled effects from protons, atomic oxygen and space debris

Figure 7 presents comparative LIDT results for samples displaying penetration holes, compression-induced cracking and cratering after simulated debris impacts. The horizontal axes respectively represent the coupling of protons and atomic oxygen, protons and debris, atomic oxygen and debris and the combination of protons, atomic oxygen and space debris. The vertical axis shows LIDT values for individual samples. These images suggest the coupled effect of three factors significantly influenced the LIDT, more so than any combination of two factors. Furthermore, the LIDTs resulting from the combined effect of three factors differed considerably from that of the coupling of protons and atomic oxygen. This difference was less notable when compared with the coupling of protons and debris or atomic oxygen and debris. This indicates the influence of debris impacts on reducing the damage threshold dominated by the combined effect of the three factors, for both the high-reflectance films shown in Figure 7(a) and the substrates shown in Figure 7(b).

Table 2. A comparison of LIDT reductions for different combinations of three space environmental factors.

Sample type	LIDT reduction		
	Proton & atomic oxygen & penetration	Proton & atomic oxygen & compression	Proton & atomic oxygen & craters
High–reflectance films	63.19%	77.35%	66.73%
Substrates	79.29%	87.73%	79.29%

Table 2 presents LIDT reductions due to different methods of interaction. These comparisons demonstrate that combined effects from three factors significantly influenced LIDTs, more so than any single-factor operation or the combination of any two factors. This indicates the combination of protons, atomic oxygen and space debris mutually enhanced destructive potential in each sample. Protons and atomic oxygen, through sputtering and penetration of the film layer, damaged the lattice structure on the film surface and within the material, leading to nano-scale or sub-nano-scale structural damage. In addition, microstructural damage caused by space debris impacts collectively acted as causative factors for laser-induced damage. A comprehensive analysis revealed that laser damage in space environments is a coupling process composed of long-term space radiation-induced degradation and sustained laser irradiation. This degradation includes sputtering by protons and atomic oxygen and micro/nano-structural damage from space debris impacts. These factors can lead to enhanced modulation of the laser field distribution, decreased structural strength, internal material fracturing and even minor-scale damage, which may be further compromised or invaded by multi-pulse laser exposure. Laser-induced damage or accelerated growth can also be induced by the transformation of stable structures

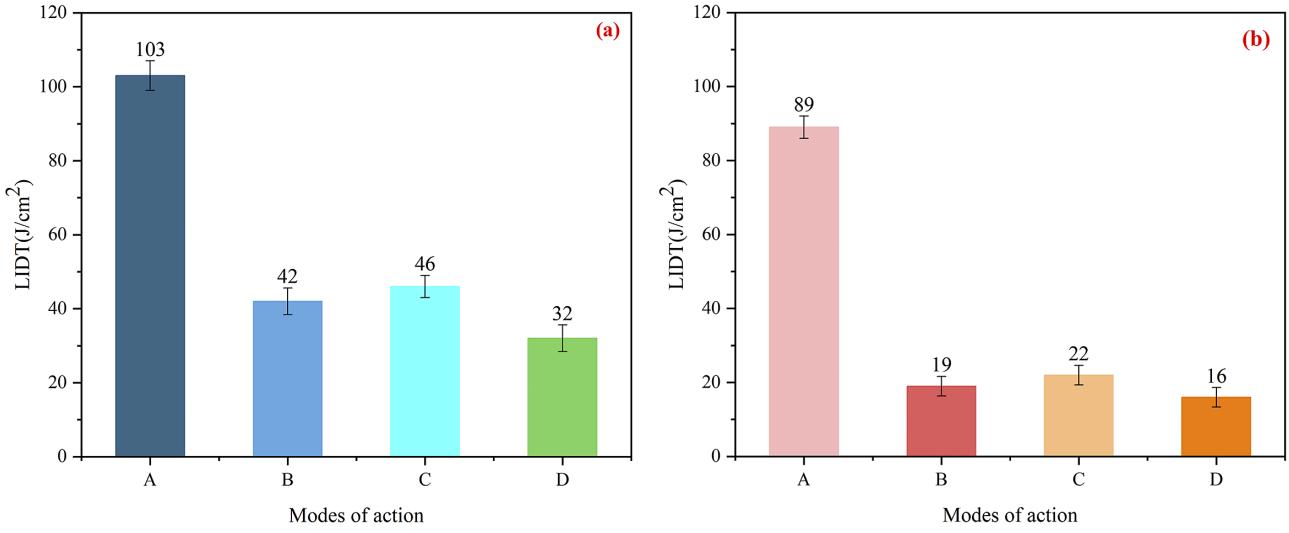

Figure 7. A comparison of LIDT values for simulated fragment compressions in (a) high-reflectance films and (b) substrates. A, protons and atomic oxygen; B, protons and penetration; C, atomic oxygen and penetration; D, protons and atomic oxygen and penetration.

into unstable structures. These factors are the primary cause of laser-induced damage and constitute vulnerable aspects that limit the operational performance of optical components in space environments.

5. Analysis and discussion

The roughness of samples was measured and compared before and after exposure to proton and atomic oxygen radiation in the same positions, to better understand the mechanisms of space radiation and the influence of laser damage on performance. In addition, high-resolution photothermal absorption testing was integrated to analyze changes in the photothermal absorption intensity of selected areas before and after exposure. Finally, computational results for proton and atomic oxygen injection were simulated using the stopping and range in ion matter (SRIM) program[36]. This simulation facilitated a quantitative analysis of transmission trajectories, concentration distributions, void distributions and energy loss curves for specific angles and entry paths within the target material.

5.1. Surface morphology

An *in situ* AFM measurement technique was used to compare microstructure differences in the same areas of high-reflectance films before and after exposure to protons and atomic oxygen radiation, the results of which are shown in Figure 8. Also, the *in situ* test results of the selected measurement area surface morphology are shown in Figure 8, where no static electric effects were observed.

A comparison of these images indicated the roughness of samples after proton irradiation was consistent at 2.33 nm before and after exposure. After atomic oxygen irradiation, roughness measurements were 2.71 nm before exposure and 2.66 nm after exposure, indicating that the space irradiation (protons and atomic oxygen) had no effects on the surface roughness.

5.2. Photothermal absorption

The photothermal absorption characteristics of materials are pivotal to the formation of damage structures. Comparing differences in photothermal absorption intensity[4] enabled the identification of potential laser damage sites and an analysis of overall film damage performance. Focusing on these samples before and after proton irradiation also facilitated a comparative analysis of changes in photothermal absorption intensity within the same region of high-reflective films at three working wavelengths, as indicated by Table 3. These results indicated that changes in photothermal absorption (before and after proton irradiation) were more sensitive than

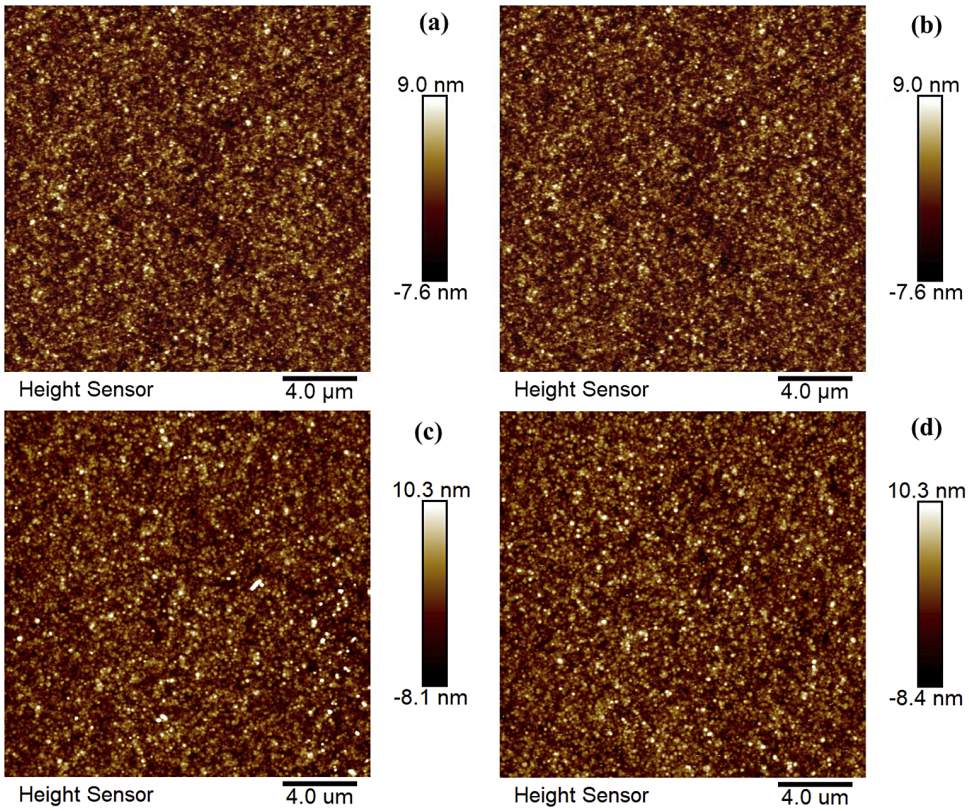

Figure 8. Surface morphology images of three-band high-reflectance thin films before and after proton and atomic oxygen irradiation: (a) before proton irradiation; (b) after proton irradiation; (c) before atomic oxygen irradiation; (d) after atomic oxygen irradiation.

Table 3. Test results for weak absorption corresponding to three operating wavelengths[39].

Wavelength (nm)	Relative values before irradiation	Relative values after irradiation	Amplification
1064	7.4	8.9	20.3%
532	5.2	6.3	21.2%
355	2.3	3.4	47.8%

AFM measurements. This increased sensitivity occurred because proton irradiation can produce nano- or sub-nano-scale strong absorption sources on the surface and subsurface of optical components (with a certain density distribution), thereby enhancing photothermal absorption. The damage induced by protons was simultaneously expected to generate minute lattice defects within the material, which may not significantly increase the photothermal absorption intensity or alter the resulting microstructure. Regardless, this effect was sufficient to produce a marked decrease in the laser damage threshold. In addition, similar changes were observed in the intensity of photothermal absorption before and after atomic oxygen irradiation.

5.3. Penetration depth

Monte Carlo simulations of incident particle penetration processes were used to further analyze irradiation effects from protons and atomic oxygen on film layers. These tests were conducted using the SRIM software, with the number of injected particles set to 10^4. Figure 9 shows concentration distributions during the penetration of 40 keV protons (Figure 9(a)) and 5 eV oxygen atoms (Figure 9(b)) onto multilayer films. The penetration depth for protons was primarily in the range of 0.35–0.48 μm, with the maximum concentration occurring at 0.42 μm. The penetration depth for atomic oxygen was primarily in the range of 0.02–0.05 μm, with the maximum concentration at 0.018 μm. The penetration depth for protons was significantly greater than that of oxygen atoms, as the number of silicon atoms produced to stop atomic oxygen was much larger than that of proton irradiation. This indicates that the stopping capability of the film layer was related to the mass of film layer atoms and incident particles, as greater incident particle masses led to stronger stopping capabilities in the film[39]. This result confirms that the microstructure and roughness of a film layer exhibited more pronounced changes relative to the protons after atomic oxygen irradiation.

The SRIM simulations also indicated that energy losses during the penetration of protons and atomic oxygen into high-reflectance films were predominantly caused by ionization energy losses. These ionization effects were prone to causing the formation of color center defects or strong absorption sources within the material, ultimately leading to laser-induced damage. Previous studies have indicated that dielectric films prepared using EB evaporation, ion-assisted deposition (IAD) and IBS coating technologies did not exhibit significant changes in their spectral curves under space particle irradiation. This is because noticeable spectral shifts occurred only in the presence of high-density color centers, leading to a reduced LIDT. In the case

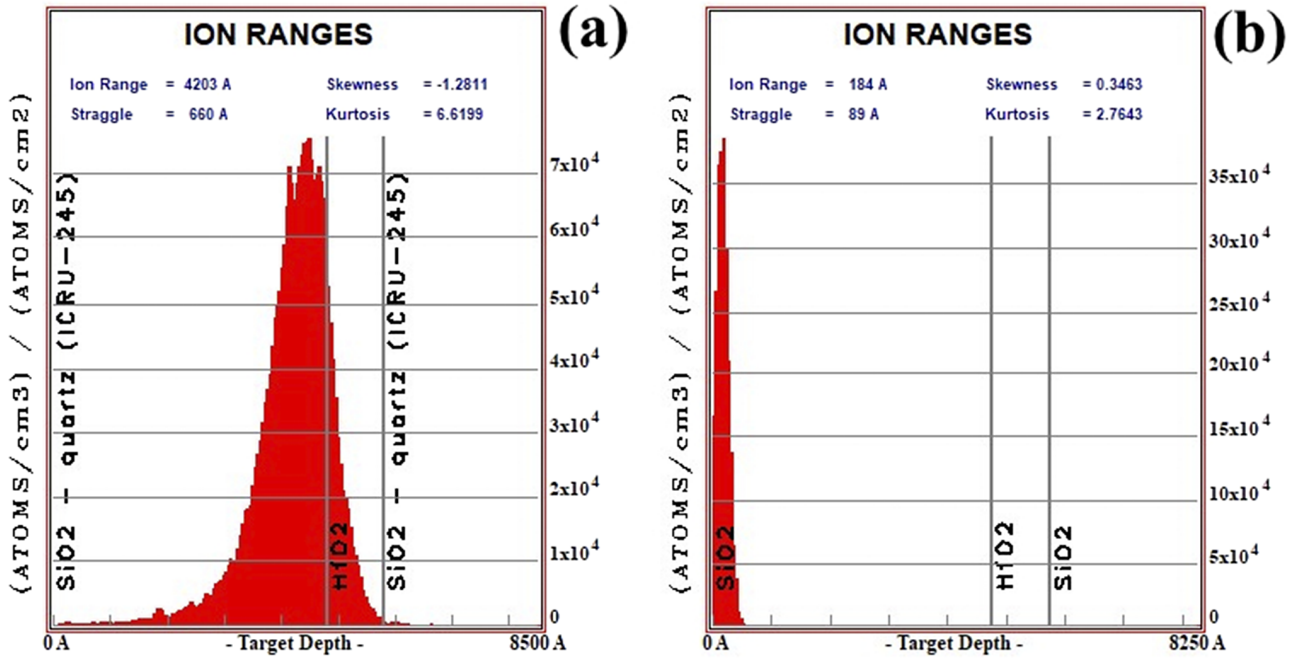

Figure 9. SRIM simulations of proton concentrations and atomic oxygen distributions within the membrane layer: (a) protons; (b) atomic oxygen.

of high-reflectance thin films and fused silica substrates, LIDT values after proton irradiation were lower than those of atomic oxygen irradiation. This was likely due to the protons penetrating to greater depths and forming larger absorption regions in deeper spatial ranges. As a result, more laser energy was deposited in this region, leading to the initiation of damage. Based on the aforementioned damage mechanisms, it is considered to use a double EB co-evaporation with ion beam-assisted method to prepare high-density, low-scattering HfO_2-SiO_2 films with high damage thresholds[40].

5.4. Fragment impact

The effects of the three simulated fragment impact modes (i.e., penetration, compression and cratering) resulted in significant damage to optical components. This damage included microscopic states (e.g., lattice defects, the generation of electron defects and chemical bond breakage), mesoscopic states (e.g., the generation and dispersion of material sub-micro/nano-particles and fragments) and macroscopic states (e.g., structural fractures and interface dislocations). These effects have been extensively studied in the field of laser damage performance and damage growth in large-sized optical components within high-power laser systems. The impact of these events significantly reduces the LIDT and damage performance. In addition, the initial damage morphology at different scales determines the damage threshold, with compression producing the lowest LIDTs, followed by penetration. LIDT changes were highest for cratering events.

6. Conclusion

A comprehensive study was conducted to investigate the effects of individual and combined actions from atomic oxygen, protons and space debris on the laser-induced damage performance of HfO_2/SiO_2 three-band high-reflection films and fused silica substrates. The absorption intensity, surface morphology, LIDT and damage evolution for three-band high-reflection films and fused silica substrates were analyzed under the separate influences of proton irradiation, atomic oxygen irradiation and space debris impacts. There were no significant changes in the spectral characteristics and microscopic morphology of components after proton and atomic oxygen irradiation, yet the results of photothermal absorption showed a noticeable increase, accompanied by a significant decrease in the LIDT. Subsequently, three different impact morphologies (penetration holes, compression cracks and crater splashing) were identified after exploring their respective influences on LIDT values. Damage evolution processes for these three morphologies exhibited similar patterns, with the size of the impact region related to the damage threshold. Generally, the larger impacts produced lower damage thresholds. The grouping and coupling effects for three space environmental factors were also investigated. Specifically, the impact of different coupling groups on LIDTs was explored for HfO_2/SiO_2 high-reflection films and fused silica substrates. These results indicated that the impact of space debris had the most significant effect on the LIDTs of optical components. The degree of material fracturing was also closely related to the corresponding damage resistance, with the compression sample exhibiting the most noticeable material fracturing. As such, these structures are more prone to damage under laser irradiation, resulting in the lowest LIDTs.

Acknowledgement

This work was supported by the National Natural Science Foundation of China (No. 61975153).

References

1. J. B. Heaney, L. R. Kauder, S. E. Bradley, and D. E. Neuberger, Proc. SPIE **4135**, 339 (2000).
2. W. Riede, H. Schroeder, P. Allenspacher, and P. Mahnke, in *Laser-induced Damage in Optical Materials* (SPIE, 2009), p. 279.
3. K. Harvey, A. Mustico, and J. Vallimont, in *Second Post-Retrieval Symposium* (1993), p. 1389.
4. A. F. Stewart and M. Finckenor, Proc. SPIE **6403**, 64030S (2007).
5. M.-J. Lan, Y.-Y. Wu, J.-M. Hu, S.-Y. He, L. Yue, J.-D. Xiao, D.-Z. Yang, Z.-W. Zhang, X.-C. Wang, Y. Qian, and M.-B. Chen, Acta Phys. Sin. **60**, 098110 (2011).
6. W. Q. Feng, Y. G. Ding, and D. K. Yan, Spacecraft Envion. Eng. **4**, 69 (2005).
7. W. Riede, P. Allenspacher, L. Jensen, and M. Jupé, in *International Society for Optics and Photonics* (2008), p. 130.
8. K. Mikami, S. Motokoshi, M. Fujita, T. Jitsuno, and K. A. Tanaka, Proc. SPIE **8190**, 81900A (2011).
9. W. Du, M. Zhu, J. Shi, T. Liu, J. Sun, K. Yi, and J. Shao, High Power Laser Sci. Eng. **11**, e61 (2023).
10. G. A. Harvey, W. H. Kinard, and J. L. Jones, in *AIAA Space 2007 Conference and Exposition* (2007), p. 1.
11. J. Du, B. Xue, J. Liu, Z. Li, T. Kobayashi, Y. Zhao, and Y. Leng, Prof. SPIE **9237**, 92371N (2014).
12. B. A. Banks, K. K. Degroh, S. K. Rutledge, and C. A. Haytas, Proc. SPIE **3784**, 62 (1999).
13. Y. Li, X. Ling, G. Wang, Y. Zhao, and J. Shao, Optik **124**, 5154 (2013).
14. Y. Cui, J. Zhao, Y. Zhao, and J. Shao, Opt. Mater. Express **6**, 3119 (2016).
15. Y. Chai, M. Zhu, K. Yi, H. Qi, and J. Shao, Proc. SPIE **9237**, 92370P (2014).
16. W. Riede, H. Schroeder, G. Bataviciute, D. Wernham, A. Tighe, F. Pettazzi, and J. Alves, Proc. SPIE **8190**, 81901E (2011).
17. N. Tajima, H. Murotani, and T. Matsudaira, Thin Solid Films **776**, 139824 (2023).
18. X. Ling, G. Wang, Y. Zhao, J. Shao, and Z. Fan, Optik **125**, 6474 (2014).

19. T. Liu, M. Zhu, W. Du, J. Shi, J. Sun, Y. Chai, and J. Shao, High Power Laser Sci. Eng. **10**, e30 (2022).
20. Y. Cui, K. Yi, Z. C. Shen, and J. D. Shao, Laser Optoelectron. Progress **49**, 040001 (2012).
21. A. K. Burnham, M. J. Runkel, S. G. Demos, M. R. Kozlowski, and P. J. Wegner, Proc. SPIE **4134**, 243 (2000).
22. S. Demos, A. Burnham, P. Wegner, M. Norton, L. Zeller, M. Runkel, M. Kozlowski, M. Staggs, and H. Radousky, Electron. Lett. **36**, 566 (2000).
23. C. Chen, Y. Wang, J. Feng, Z. Wang, Y. Chen, Y. Lu, Y. Zhang, D. Li, Y. Cui, and J. Shao, Opt. Mater. **136**, 113349 (2023).
24. D. Schwam and M. H. Litt, Adv. Performance Mater. **3**, 153 (1996).
25. T. S. Rose, M. S. Hopkins, and R. A. Fields, IEEE J. Quantum Electron. **31**, 1593 (1995).
26. F. Y. Génin, A. Salleo, T. V. Pistor, and L. Chase, J. Opt. Soc. Am. A **18**, 2607 (2001).
27. P. E. Miller, J. D. Bude, T. I. Suratwala, N. Shen, T. A. Laurence, W. A. Steele, J. Menapace, M. D. Feit, and L. L. Wong, Opt. Lett. **35**, 2702 (2010).
28. B. Ma, Z. Li, M. L. Lu, K. Wang, and H. F. Jiao, Appl. Opt. **55**, 7078 (2016).
29. L. Gallais, J.-Y. Natoli, and C. Amra, Opt. Express **10**, 1465 (2002).
30. S. Baccaro, A. Piegari, D. Sarcina, and A. Cecilia, in *IEEE Symposium Conference Record Nuclear Science* (2004), p. 769.
31. X. Gao, S. Yang, Y. Wang, J. Wang, and Z. Feng, Atomic Energy Sci. Technol. **44**, 228 (2010).
32. J. Cheng, Y. Niu, J. Wang, P. Qu, and P. Zhang, Opt. Techn. **44**, 651 (2018).
33. E. Pace, A. Pini, G. Corti, F. Bogani, A. Vinattieri, C. Pickles, and R. Sussmann, Diamond Related Mater. **10**, 736 (2001).
34. W. Wang, B. Dai, Y. Wang, G. Shu, K. Yao, B. Liu, J. Zhao, K. Liu, L. Yang, J. Zhu, and J. Han, Mater. Sci. Technol. **28**, 42 (2020).
35. J. DiJon, J. Hue, A. Disgecmez, E. Quesnel, and B. Rolland, Proc. SPIE **2714**, 416 (1995).
36. X. Cheng, T. Ding, W. He, J. Zhang, H. Jiao, B. Ma, Z. Shen, and Z. Wang, Proc. SPIE **8190**, 31 (2011).
37. R. A. Negres, C. J. Stolz, G. Batavičiūtė, and A. Melninkaitis, Proc. SPIE **11514**, 115140L (2020).
38. M. D. Feit and A. M. Rubenchik, Proc. SPIE **5273**, 264 (2003).
39. S. Guan, Q. Yu, Y. Li, Y. N. Wang, K. Wang, J. Q. Han, X. S. Niu, and M. Bin, Spacecraft Environ. Eng. **39**, 69 (2022).
40. X. Niu, H. Jiao, G. Bao, J. Zhang, X. Cheng, and Z. Wang, Proc. SPIE **10447**, 1044726 (2017).